Giant Nonlinear Optical Activity in Two-Dimensional Palladium Diselenide

Juan YU
Central South University and Hangzhou Dianzi University
Xiaofei KUANG
Hangzhou Dianzi University
Junzi Li
Shenzhen University
Jiahong Zhong
Central South University
Cheng Zeng
Central South University
Lingkai Cao
Central South University
Zongwen Liu
The University of Sydney https://orcid.org/0000-0002-6434-1643
Zhouxiaosong Zeng
Hunan University
Ziyu Luo
Hunan University
Tingchao He (tche@szu.edu.cn)
Shenzhen University
Anlian Pan (anlian.pan@hnu.edu.cn)
Hunan University https://orcid.org/0000-0003-3335-3067
Yanping LIU (liuyanping@csu.edu.cn)
Central South University https://orcid.org/0000-0003-2990-3783

Article

Keywords: nonlinear optoelectronic devices, transition metal chalcogenides, palladium diselenide flakes

Posted Date: July 28th, 2020

DOI: https://doi.org/10.21203/rs.3.rs-38019/v1

Version of Record: A version of this preprint was published at Nature Communications on February 17th, 2021. See the published version at https://doi.org/10.1038/s41467-021-21267-4.

Giant Nonlinear Optical Activity in Two-Dimensional Palladium Diselenide

Juan Yu[1,2,3,#], Xiaofei Kuang[3,#], Junzi Li[4,#],Jiahong Zhong[1,2], Cheng Zeng[1,2], Lingkai Cao[1,2], Zongwen Liu[5], Zhouxiaosong Zeng[6], Ziyu Luo[6], Tingchao He[4,*], Anlian Pan[6,*], & Yanping Liu[1,2,7*]

1. *School of Physics and Electronics, Hunan Key Laboratory for Super-microstructure and Ultrafast Process, Central South University, 932 South Lushan Road, Changsha, Hunan 410083, P. R. China*
2. *State Key Laboratory of High-Performance Complex Manufacturing, Central South University, 932 South Lushan Road, Changsha, Hunan 410083, P. R. China*
3. *School of Electronics and Information, Hangzhou Dianzi University,1158 Second Street, Xiasha College Park, Hangzhou, Zhejiang, 310018, P. R. China*
4. *College of Physics and Optoelectronic Engineering, Shenzhen University, Shenzhen 518060, P. R. China*
5. *School of Chemical and Biomolecular Engineering, The University of Sydney, NSW 2006, Australia*
6. *College of Materials Science and Engineering, Hunan University，Changsha, Hunan 410082, P. R. China*
7. *Shenzhen Research Institute of Central South University, A510a, High-tech Industrial Park, Yuehai Street, Shenzhen 518057,P. R. China*

Abstract

Nonlinear optical (NLO) effects in layered atomically thin two-dimensional (2D) materials provide a promising prospect for multifarious optoelectronic applications. The NLO characteristics of transition metal chalcogenides (TMDCs) are attracting growing attention and have been extensively explored recently. However, these materials possess sizable bandgaps ranging from visible to ultraviolet regions, so the investigation of narrow-bandgap materials remains deficient. Here, we report our comprehensive study on the NLO processes in palladium diselenide ($PdSe_2$) flakes that have a near-infrared bandgap. Interestingly, this material exhibits a unique thickness-dependent second harmonic generation (SHG) feature, embodied in the strong (negligible) SHG signals in even (odd) layers, in contrast with that of other TMDCs. Furthermore, the two-photon absorption (TPA) coefficients (β ~4.5×10^5, 2.83×10^5, 1.7×10^5, and 1.85×10^4 cm/GW) of 1-3 L and bulk $PdSe_2$ are larger by two and three orders of magnitude, compared with that of the conventional 2D materials. Significantly, at the excitation wavelength of 600 nm, a robust saturable absorption with giant modulation depths (α_s ~47%, 30%, and 41%) was observed in 1-3 L $PdSe_2$, which has yet been obtained in other 2D materials. Such unique NLO characteristics enable $PdSe_2$ to be a potential candidate for technological innovations in nonlinear optoelectronic devices.

* Correspondence and requests for materials should be addressed to Email: liuyanping@csu.edu.cn; anlian.pan@hnu.edu.cn; tche@szu.edu.cn

Introduction

Nonlinear optical (NLO) properties play an increasingly significant role in the development of laser technology, optical spectroscopy, and material structure analysis [1-4]. Recently, the study of NLO activity in 2D layered materials (graphene, TMDCs, and black phosphorus (BP)) has come into being a new category of photonic nanomaterials and made significant evolvement [5-9]. Graphene is the initial ignition of atomically thin 2D materials and its extraordinary nonlinearities, including saturable absorption (SA) [10, 11], optical limiting [12], and harmonic generation [13], have gathered great interest. However, the inherent zero-bandgap, centrosymmetric crystal structure [14] of graphene hinders the study of their NLO effects, including second harmonic generation (SHG) and multiphoton absorption features. Conversely, BP possesses intrinsic anisotropy and layer-dependent direct bandgap that can be adjusted from 0.3 to 2 eV [15, 16], leading to high SA modulation depths (~27.6% at 400 nm, ~ 12.4% at 800 nm [17]) and large two-photon absorption (TPA) coefficient ($(-6.98\pm 0.6) \times 10^3$ cm/GW [18]). However, BP lacks sufficient air stability, resulting in the rapid degradation of its NLO properties. Meanwhile, the most studied TMDCs materials (MX_2, M=Mo, W, and X=S, Se, Te), revealing various fascinating NLO activities, such as SHG, SA, and TPA, have the sizable bandgap ranging from visible to ultraviolet region (1~2.5 eV) and are short of narrow-bandgap materials [19]. Interestingly, $PdSe_2$ is a novel pentagonal 2D material with robust anisotropy, high carrier mobility, and air stability, which gives it considerable advantages in nonlinear optoelectronic devices [20]. In addition, $PdSe_2$ has a modifiable thickness-dependent bandgap from 0.03 to

1.37 eV [21], filling the interspace between zero-gap graphene and large-gap TMDCs. However, to date, the NLO activity of $PdSe_2$ flakes has rarely been explored. An extensive and in-depth study of the NLO behavior of $PdSe_2$ is of great significance for the expansion of its optical applications.

Herein, we fabricate large-size $PdSe_2$ flakes with different layers and perform a comprehensive investigation of thickness-dependent NLO properties of $PdSe_2$ flakes. Extraordinarily, owing to its unique layer-dependent inversion symmetry, $PdSe_2$ exhibits an SHG behavior that is totally opposed to that in other 2D materials [22, 23]. Moreover, the $PdSe_2$ flakes exhibit giant TPA coefficients (β) that are two or three orders of magnitude larger compared with conventional semiconductors [24-26]. Importantly, excellent saturable absorption is observed in 1-3 L $PdSe_2$, with their modulation depths (α_s) much higher than most of the other 2D materials [27-29]. Our observations not only provide profound insights for the NLO features in this innovative nanomaterial, but also open a new avenue for the future nonlinear optoelectronic application.

Results and Discussion

Crystal structure and characterization of few-layer $PdSe_2$ flakes. The unique structure of $PdSe_2$ enables its innovative optical characteristics. $PdSe_2$ holds a stratiform structure that is identical to other 2D materials (graphene, hBN, black phosphorus, TMDCs), as shown in Figure 1a. Pd and Se atoms combine to form a covalent bond within a monolayer, and VdWs force dominates the interactions between adjacent layers. In the side view, $PdSe_2$ exhibits a unique plicate crystal structure with a

monolayer vertical plicate height of 1.604 Å. In comparison to the traditional 2D materials with highly symmetric hexagonal honeycomb structure, the Pd and Se atoms of $PdSe_2$ constitute an asymmetric pentagonal structure (Figure 1b). The ultrathin $PdSe_2$ crystal displays robust interlayer coupling with the relatively large binding energy of 190 meV/atom [30], also manifested in the process of mechanical exfoliation. Monolayer and few-layer $PdSe_2$ is difficult to be obtained by the conventional scotch tape method. Here, the gold-assisted exfoliation method is adopted to acquire monolayer and few-layer $PdSe_2$ with large size onto the Si/SiO_2 substrates, as shown in Figure 1c, 2a, and 2c. Recently, Raman technology demonstrated excellent performance in determining the layer number of various 2D materials. Through analyzing the Raman spectrum, the layer number of samples can be identified fleetly, precisely, and non-destructively. Based on it, the Raman spectra of the obtained 1-6 L and bulk $PdSe_2$ samples at a wavenumber range of 0-300 cm^{-1} were performed to estimate the layer number (Figure 1d). Obviously, the Raman peak position varies gradually as the layer number increases. It is worth mentioning that Raman peaks in the low-frequency region (0-100 cm^{-1}) vary by a large margin. The low-frequency Raman modes indicate the interlayer vibrations of samples, and it is robust, even exceeding the high-frequency modes (100-300 cm^{-1}), which is ascribed to the strong interlayer coupling of $PdSe_2$. Because of the significant shifts of low-frequency Raman modes, the layer number can be determined precisely. The feasibility and specific operation of such results have been reported in detail in the previous works of authors [21].

Second Harmonic Generation properties of $PdSe_2$ flakes. To better understand the

NLO characteristics of this material, the SHG properties of few-layer $PdSe_2$ at the excitation wavelength of 800 nm were studied in detail. For the monolayer region, the detected SHG signal was negligible. While the laser spot was switched to the bilayer area, strong signals could be observed at 400 nm. In order to further demonstrate the dependence of SHG signals on the $PdSe_2$ layer number, the spatial mapping was implemented. The red boxes in Figure 2a and c indicated the scanning regions of the sample, containing 1-8 L and bulk $PdSe_2$ flakes to ensure that the test specimen is sufficient. Clearly, the even layers of $PdSe_2$ emit a strong SHG signal, while that of the odd-numbered layers and the bulk is almost negligible (Fig. 2b and d). Such a result is exactly opposite to the SHG phenomenon presented in other groups VI 2D materials, which shows a strong SHG signal in the odd layers and no signal in the even layers [22, 23, 31]. It is well known that strong SHG signals will occur only in 2D materials with broken inversion symmetry [32]. Interestingly, the odd-numbered layers of $PdSe_2$ belong to the C_{2h} (2/m) point group and $P2_1/c$ (No.14) space group, which have inversion symmetry. The even-numbered layers possess the C_{2v} (mm2) point group and $Pca2_1$ (No. 29) space group with broken inversion symmetry. Meanwhile, the bulk $PdSe_2$ is an orthogonal structure with the D_{2h} point group and Pbca (No. 61) space group with inversion symmetry [20]. Unlike other 2D materials, whose even layer has inversion symmetry, and that is broken in the odd layer, $PdSe_2$ presents just the opposite properties. That results in the unique layer dependence of the SHG signal. Additionally, the uniformity of the sample is excellent, attributing to the gold-assisted exfoliation method.

Generally, there are many factors influencing the SHG intensity of $PdSe_2$, among which the excitation wavelength is a relatively significant one. To figure out which wavelength can generate the highest SHG signal, the SHG spectra excited at the wavelengths of 780-1000 nm at a step length of 20 nm were performed. As shown in Figure 3a, there are strong excitation wavelength-dependent SHG signals. The highest SHG signal was observed under 880 nm excitation. In addition, excited with the same wavelength, the layer-dependent SHG signals in $PdSe_2$ were measured. It was found that the odd-numbered layers (1, 3, 5, and 7 L) exhibited the lower SHG intensities while the higher intensities are observed in the even-numbered layers (2, 4, 6 and 8 L). The SHG intensities as a function of the layer numbers were compared (inset in Figure 3b), and it can be seen that the highest SHG intensity emerged in 4 L. In general, the NLO process of a crystal can be expressed by the relationship of polarization vector and the electric field of the incident light presented as [1, 2]

$$P = \varepsilon_0\left(\chi E + \chi^{(2)}E^2 + \chi^{(3)}E^3 + \cdots\right), \quad (1)$$

Where P is the polarization vector, ε_0 is the permittivity in a vacuum, χ is the electric susceptibility of the medium, and E is the electric field component of the incident light. Corresponding to the SHG process, the dominated term is E^2. To confirm the SHG mechanism, the correlation between the detected SHG intensity and the excitation intensity was measured. As presented in Figure 3c, it was found that the SHG intensity is quadratically dependent on the excitation power, providing direct evidence for the SHG mechanism.

Besides, the polarization-resolved SHG signals were also performed, with the aim

to identify the crystal orientation of the sample. In our measurement, the polarization orientation of the incident and detected light was parallel (For the specification, see Experimental details). Under parallel configuration, the polar plot of the SHG signal represents distinct anisotropy, embodied in the dumbbell shape of the polar plot (Figure 3d). The minimum SHG intensity appears at 0°, which gradually increases as the polarization orientation rotates, while the maximal intensity appears at 90° or so. The slight skewing of the polar plot may result from the distorted crystal lattice. Confronted with the experimental results, we use the nonlinear dielectric susceptibility tensor to analyze the SHG polar plot. The SHG polarization vector can be affected by the electrical field intensity of the incident light as expressed：

$$\boldsymbol{P} = d\boldsymbol{E} \tag{2}$$

Where $\boldsymbol{P}$ is the SHG polarization vector, d is the dielectric susceptibility tensor, and $\boldsymbol{E}$ is the electrical field intensity of the incident light. Under the three-dimensional geometric space, $\boldsymbol{P}$ and $\boldsymbol{E}$ have three components in the x, y, and z-direction, respectively. Likewise, other variables should also have a three-dimensional form. Therefore, the above formula can be expressed as follows

$$\begin{pmatrix} P_x \\ P_y \\ P_z \end{pmatrix} = \begin{pmatrix} d_{11} & d_{12} & d_{13} & d_{14} & d_{15} & d_{16} \\ d_{21} & d_{22} & d_{23} & d_{24} & d_{25} & d_{26} \\ d_{31} & d_{32} & d_{33} & d_{34} & d_{35} & d_{36} \end{pmatrix} \begin{pmatrix} E_x E_x \\ E_y E_y \\ E_z E_z \\ 2E_y E_z \\ 2E_x E_z \\ 2E_x E_y \end{pmatrix} \tag{3}$$

Where d_{ij} is the element of the dielectric susceptibility tensor. For the experimental backscattering setup, the electrical field intensity of the incident light in the z-direction was negligible. Thus, the electrical field intensity in the x and y directions can be

expressed as

$$E_x = E_0 \cos\theta$$
$$E_y = E_0 \sin\theta \quad (4)$$

Where E_0 is the module of the electrical field intensity of the incident light, and θ is the angle between the x-axis of the crystal lattice of $PdSe_2$ and the polarization orientation of the incident light. Under the parallel backscattering configuration, the eventual SHG intensity was only correlated with P_x and P_y as expressed

$$I_{\parallel} \propto \left(P_x \cos\theta + P_y \sin\theta\right)^2 \quad (5)$$

Where $I_{\parallel}$ is the detected SHG intensity under the parallel configuration. Substitute Eq (3) to Eq (5), we obtained

$$I_{\parallel} \propto [d_{11}\cos\theta^3 + (d_{21} + 2d_{16})\cos\theta^2 \sin\theta + (d_{12} + 2d_{26})\cos\theta \sin\theta^2 + d_{22}\sin\theta^3]^2 \quad (6)$$

Using this formula, the experimental SHG intensities are fitted appropriately, as shown in the solid red curve in Figure 3d. It can be seen that the experimental results are quite consistent with the theoretical analysis. Meanwhile, the polarization-resolved SHG measurements are expected to accurately identify the crystal orientation of $PdSe_2$ on the macro scale.

TPA properties of $PdSe_2$ flakes. The NLO processes in 2D materials can be divided into two classifications, parametric and non-parametric processes [33]. The parametric process in 2D materials is mainly a scattering process, which describes that the ground state is excited into a virtual state, and there is no electron transfer and absorption between the two virtual states, such as the SHG above. On the contrary, the non-

parametric process describes the excitation from the ground state to a real state, which involves absorption and electron transfer, mainly including TPA and SA. To deeply explore the NLO properties of $PdSe_2$, its TPA was further investigated. Above all, the monolayer and few-layer $PdSe_2$ flakes were obtained from the bulk crystal by gold-assisted exfoliation, which was then transferred to the transparent quartz substrates. After that, their TPA was measured using a nonlinear transmittance method. According to our previous reports, $PdSe_2$ exhibits novel linear dichroism features under the excitation of 300-800 nm [21]. When the excitation wavelength is 800 nm, the linear absorption is almost negligible in the solid film. Consequently, TPA could be predictable when excited by pulses at 800 nm. As intuitively described in Figure 4, the transmittance of the $PdSe_2$ flakes decreases with the increasing incident light intensity, exhibiting a typical TPA characteristic.

Based on the nonlinear transmission method, the TPA coefficient of the samples could be determined by the following formula [34]:

$$T(I_0) = \frac{I_t}{I_0} = \frac{[\ln(1 + I_0 d\beta)]}{I_0 d\beta} \tag{7}$$

Where $T(I_0)$ is the transmittance of the $PdSe_2$ flakes, I_t is the transmitted light intensity of the sample, I_0 is the incident irradiance intensity, β is the TPA nonlinear absorption coefficient, and d is the thickness of the $PdSe_2$ flakes. By fitting the experimental data with Eq.7, the β values of 1, 2, 3 L, and bulk were determined to be 4.5×10^5, 2.83×10^5, 1.7×10^5, and 1.85×10^4 cm/GW, respectively, which are two or three

orders of magnitude larger compared with other conventional semiconductors, such as MoS_2, WS_2, GaAs, CdS, and ZnO [24-26], implying their potential TPA-based applications. Such giant TPA coefficients may originate from the strong exciton effects in $PdSe_2$ [35]. In addition, it was found that the TPA coefficient of $PdSe_2$ gradually decreases with the increasing layer number. Such a phenomenon is mainly attributed to the fact that the bandgap decreases with the increase of layer number, and there is a certain detuning between the formative exciton and the two-photon energy [36].

SA properties of $PdSe_2$ flakes. Considering strong SA was widely reported in various two-dimensional TMDCs, including MoS_2 [37], WS_2 [38], WSe_2 [39], and $MoSe_2$ [40], typical SA may also be expected in our $PdSe_2$ in the case of 600 nm excitation. The normalized transmittance versus the incident intensity in 1-3 L and bulk $PdSe_2$ is presented in Figure 5, which can be fitted, according to a standard model of SA, as shown in the following formula [41]:

$$T(I_0) = 1 - \frac{\alpha_s}{1 + \frac{I_0}{I_s}} - \alpha_u \tag{8}$$

Where α_s is the modulation depth, I_s is the saturable intensity, and α_u is the unsaturated absorption components. And the fitting parameters of the modulation depths α_s of 1-3L $PdSe_2$ are 47%, 30% and 41%, respectively. The saturable intensity (often indicating the half of the highest optical absorption) of 1-3 L $PdSe_2$ is 0.98, 1.1, and 1.2 GW/cm^2, respectively. As the sample thickens, the saturable intensity gradually increases. The modulation depths α_s are much higher than most of the other 2D materials, such as SnSe [27], $MoSe_2$ [28], MoS_2 [29], which can be a promising advantage for the application in ultrafast lasers. The high modulation depths mainly

result from the low unsaturated loss, indicating a low defect density in the $PdSe_2$ [7]. However, the modulation depths in bulk (thinner) and few-layer $PdSe_2$ (only 2.8%) are much lower than that in 1-3 L $PdSe_2$, which may be attributed to the increased unsaturated loss induced by the strengthened scattering [7]. It is worth noting that for the extremely thick bulk $PdSe_2$, the SA phenomenon disappeared. For the sample that is thick enough, the light capacity is sufficient and the saturation state will not be easily reached. The excellent SA property of 1-3 L $PdSe_2$ endows its application prospect in the field of ultrafast lasers.

To understand the principle of the transmittance dependence on the incident irradiance, the electronic transition process in the momentum space should be clear. Figure 5e illustrates the electronic transition process of SA. The bandgap of the monolayer (bulk) $PdSe_2$ is determined to be 1.37 (0.03) eV, and it presents unusual indirect bandgap characteristics. In our case, the energy of the incident photon (2.06 eV) is much larger than the bandgap of a few-layer $PdSe_2$. For low excitation intensity, the electrons in the valence band jumped to the relatively high energy levels in the conduction band, as illustrated on the left panel of Figure 5e. Then, the hot electrons relaxed to the lower energy band, and populated in the bottom of the conduction band. With the increasing incident optical intensity, the excited electrons also increased. Electron is a fermion, which cannot populate at the same energy level. Thus, the energy levels were gradually filled from the bottom to the top in the conduction band (middle panel in Figure 5e). When the incident optical intensity further increased, the electrons almost filled the most energy levels. Owing to the Pauli exclusion principle, the

electrons can hardly populate in the new energy levels. Thus, the electronic transition process was impeded. The number of the absorbed photons gradually approached saturation, as indicated on the bottom panel of Figure 5e. This explains the gradually saturable transmittance with the increased incident optical intensity in the experiment.

Conclusion

We have successfully fabricated large-area $PdSe_2$ flakes with different thicknesses on the Si/SiO_2 and quartz substrates. Significantly, robust broadband SHG properties in the even layers $PdSe_2$ were demonstrated, because of the unique anisotropic puckered pentagonal structure, in contrast with other 2D materials. Besides, we investigated the TPA and SA characteristics of $PdSe_2$ flakes. Under the excitation at 800 nm, 1-3 L and bulk $PdSe_2$ exhibited giant TPA coefficients (β) of 4.5×10^5, 2.83×10^5, 1.7×10^5, and 1.85×10^4 cm/GW, which are at least two orders of magnitude larger than that of conventional semiconductors. Interestingly, when the excitation was switched to 600 nm, on account of the ultra-low unsaturable loss, strong SA with the modulation depths (α_s) up to 47%, 30% and 41% for 1-3 L $PdSe_2$ were observed. These results are among the largest levels obtained in other traditional 2D materials. Such prominent NLO activity of 2D $PdSe_2$ offers insights into its potential application in optical switching, ultrafast lasers, saturation absorbers, optical limiters, and micro/nano optical modulation devices.

Experimental details

Sample preparation. The $PdSe_2$ flakes were exfoliated from bulk single-crystal $PdSe_2$ (HQ graphene) onto silicon substrates and transparent substrates, using gold-assisted

exfoliation. The thickness of the 1, 2, 3 L, and bulk $PdSe_2$ are 0.6, 1.2, 1.8, and 10 nm, respectively.

Raman single spectrum characterization. A WITec Alpha 300R was utilized to obtain the high-resolution spectra. A 532 nm laser was used to excite the $PdSe_2$ flakes with a power of 0.25 mW, a 100× objective with NA = 0.9, and a laser spot size of 1 μm. The integration time is 5 s and accumulated 10 times to obtain a high signal-to-noise ratio. The 1800 g/mm optical grating was used to improve the spectral resolution.

SHG measurements and characterization. The reflective geometry with normal incidence excitation was used to achieve the SHG measurement. For SHG mapping characterization, the region of 40×40 μm^2 and 50×50 μm^2 containing 1-8 L $PdSe_2$ flakes was selected. A fiber-based pulsed laser was selected as the fundamental pump source with the center wavelength at 800 nm. The laser pulses were focused onto a spot size of 2 μm on the $PdSe_2$ sample by a 50× objective with NA=0.55. The same objective lens was used to collect the SHG signal scattered from the sample and then detected by the CCD spectrometer. The integration time of 0.5 s and the scan duration of 2 hours was set to achieve the high-resolution mapping images.

For the measurements of layer number dependent SHG signal, the excitation wavelength was fixed at 880 nm, and the same excitation intensity was used. For SHG polarization measurement, a half-wave plate (analyzer) was placed in the incident (outgoing) light path. Only the light whose polarization orientation was parallel to the optical axis of the analyzer can pass to be detected by a charged coupling device (CCD). And the parallel configuration with the step size of 10° was adopted.

TPA and SA measurements. The TPA and SA of $PdSe_2$ were measured using the nonlinear transmittance method in a home-built micro NLO system. The samples were excited at the wavelengths of 600 nm (spectral width ~ 15 nm) or 800 nm (spectral width ~ 10 nm) by the laser pulses from an OPA combined with TOPAS (1000 Hz, 110 fs, Spectra-Physics, Inc.). The femtosecond pulses were focused onto the sample by A 50× objective lens with NA=0.55, and the spot size at the focal point was ~ 2 μm.

Authors contributions

YPL, ALP, and TCH, conceived and supervised the project. JY fabricated the device and performed the Raman characterizations. JZL, ZXSZ, and ZYL performed the nonlinear optical measurements. YPL, JY, XFK, CZ, JHZ, LCC, ZWL, and TCH provided a vital interpretation of the data. YPL, TCH, and JY drafted the paper. All authors read and polished the revised manuscript. JY, XFK, and JZL contribute equally to this work.

Acknowledgments

The authors acknowledge support from the National Natural Science Foundation of China (Grant No. 61775241), the Youth Innovation Team (Grant No:2019012) of CSU, the Science and Technology Innovation Basic Research Project of Shenzhen (Grant No. JCYJ20180307151237242), Hunan Provincial Science Fund for Distinguished Young Scholars(Grant No: 2020JJ2059), and the Hunan province key research and development project (Grant No.2019GK2233). The authors also are grateful to the support by the Project of State Key Laboratory of High-Performance Complex Manufacturing, Central South University (Grant No. ZZYJKT2020-12).

Competing interests

The authors declare that they have no competing interests.

References

1. M. Levenson, "The principles of nonlinear optics," IEEE Journal of Quantum Electronics **21**, 400-400 (1985).
2. R. M. Barry and W. B. Robert, "Book Review: Nonlinear Optics, Third Edition," Journal of Biomedical Optics **14**, 1-4 (2009).
3. Y. R. Shen, "Surface properties probed by second-harmonic and sum-frequency generation," Nature **337**, 519-525 (1989).
4. N. Bloembergen, "Nonlinear optics and spectroscopy," Reviews of Modern Physics **54**, 685-695 (1982).
5. F. Xia, T. Mueller, Y.-m. Lin, A. Valdes-Garcia, and P. Avouris, "Ultrafast graphene photodetector," Nature Nanotechnology **4**, 839-843 (2009).
6. L. Ju, B. Geng, J. Horng, C. Girit, M. Martin, Z. Hao, H. A. Bechtel, X. Liang, A. Zettl, Y. R. Shen, and F. Wang, "Graphene plasmonics for tunable terahertz metamaterials," Nature Nanotechnology **6**, 630-634 (2011).
7. Q. Bao, Y. Wang, Z. Ni, Y. Yan, Z. Shen, K. Loh, and D. Tang, "Atomic-Layer Graphene as a Saturable Absorber for Ultrafast Pulsed Lasers," Advanced Functional Materials **19**(2009).
8. D.-S. Tsai, K.-K. Liu, D.-H. Lien, M.-l. Tsai, C.-F. Kang, C.-A. Lin, L. Li, and J.-H. He, "Few-Layer MoS2 with High Broadband Photogain and Fast Optical Switching for Use in Harsh Environments," ACS nano **7**(2013).
9. W.-J. Liu, M. Liu, Y. OuYang, H. Hou, G. Ma, M. Lei, and Z. Wei, "Tungsten diselenide for mode-locked erbium-doped fiber lasers with short pulse duration," Nanotechnology **29**(2018).
10. Z. Sun, T. Hasan, and A. C. Ferrari, "Ultrafast lasers mode-locked by nanotubes and graphene," Physica E: Low-dimensional Systems and Nanostructures **44**, 1082–1091 (2012).
11. A. Martinez and Z. Sun, "Nanotube and graphene saturable absorbers for fibre lasers," Nature Photonics **7**, 842-845 (2013).
12. J. Wang, Y. Chen, l. Rihong, H. Dong, Y. Ju, J. He, J. Fan, K. Wang, K.-S. Liao, L. Zhang, S. Curran, and W. Blau, "Graphene and Carbon Nanotube Polymer Composites for Laser Protection," JOURNAL OF INORGANIC AND ORGANOMETALLIC POLYMERS AND MATERIALS **21**, 736-746 (2011).
13. N. Kumar, J. Kumar, C. Gerstenkorn, R. Wang, H.-Y. Chiu, A. L. Smirl, and H. Zhao, "Third harmonic generation in graphene and few-layer graphite films," Physics (2013).
14. R. Raveendran-Nair, P. A. Blake, A. N. Grigorenko, K. S. Novoselov, T. Booth, T. Stauber, N. Peres, and A. K. Geim, "Fine Structure Constant Defines Visual Transparency of Graphene," Science (New York, N.Y.) **320**, 1308 (2008).
15. V. Tran, R. Soklaski, Y. Liang, and L. Yang, "Layer-Controlled Band Gap and Anisotropic Excitons in Phosphorene," Physical Review B **89**(2014).
16. L. Li, J. Kim, C. Jin, G. Ye, D. Qiu, F. Da Jornada, Z. Shi, L. Chen, Z. Zhang, F. Yang, K. Watanabe, T. Taniguchi, W. Ren, S. Louie, X. Chen, Y. Zhang, and F. Wang, "Direct Observation of Layer-Dependent Electronic Structure in Phosphorene," Nature Nanotechnology **12**(2016).

17. S. Lu, L. Miao, Z. Guo, X. Qi, C. Zhao, S. Wen, D. Tang, and D. Fan, "Broadband nonlinear optical response in multilayer black phosphorus: An emerging infrared and mid-infrared optical material," Opt. Express **23**(2015).
18. R. Chen, Y. Tang, X. Zheng, and T. Jiang, "Giant nonlinear absorption and excited carrier dynamics of black phosphorus few-layer nanosheets in broadband spectra," Appl. Opt. **55**, 10307-10312 (2016).
19. K. Mak and J. Shan, "Photonics and optoelectronics of 2D semiconductor transition metal dichalcogenides," Nature Photonics **10**, 216-226 (2016).
20. A. D. Oyedele, S. Yang, L. Liang, A. A. Puretzky, K. Wang, J. Zhang, P. Yu, P. R. Pudasaini, A. W. Ghosh, Z. Liu, C. M. Rouleau, B. G. Sumpter, M. F. Chisholm, W. Zhou, P. D. Rack, D. B. Geohegan, and K. Xiao, "PdSe2: Pentagonal Two-Dimensional Layers with High Air Stability for Electronics," Journal of the American Chemical Society **139**, 14090-14097 (2017).
21. J. Yu, X. Kuang, Y. Gao, Y. Wang, K. Chen, Z. Ding, J. Liu, C. Cong, J. He, Z. Liu, and Y. Liu, "Direct Observation of the Linear Dichroism Transition in Two-Dimensional Palladium Diselenide," Nano Letters **20**, 1172-1182 (2020).
22. L. Malard, T. Alencar, A. Barboza, K. Mak, and A. de Paula, "Observation of intense second harmonic generation from MoS2 atomic crystals," Physical review. B, Condensed matter **87**, 201401(R) (2013).
23. Y. Li, Y. Rao, K. F. Mak, Y. You, S. Wang, C. R. Dean, and T. F. Heinz, "Probing Symmetry Properties of Few-Layer MoS2 and h-BN by Optical Second-Harmonic Generation," Nano Letters **13**, 3329-3333 (2013).
24. S. Zhang, N. Dong, N. McEvoy, M. O'Brien, S. Winters, N. Berner, C. Yim, X. Zhang, Z. Chen, L. Zhang, G. Duesberg, and J. Wang, "Two photon absorption and its saturation of WS2 and MoS2 monolayer and few-layer films," (2015).
25. Y. Li, N. Dong, S. Zhang, X. Zhang, Y. Feng, K. Wang, L. Zhang, and J. Wang, "Giant Two-Photon Absorption in Monolayer MoS2," Laser & Photonics Review **9**, 427-434 (2015).
26. C. Cirloganu, L. Padilha, D. Fishman, S. Webster, D. Hagan, and E. Van Stryland, "Extremely nondegenerate two-photon absorption in direct-gap semiconductors [Invited]," Opt. Express **19**, 22951-22960 (2011).
27. C. Zhang, H. Ouyang, R. Miao, Y. Sui, H. Hao, Y. Tang, J. You, X. Zheng, Z. Xu, X. a. Cheng, and T. Jiang, "Anisotropic Nonlinear Optical Properties of a SnSe Flake and a Novel Perspective for the Application of All-Optical Switching," Advanced Optical Materials **7**, 1900631 (2019).
28. Z. Luo, Y. Li, M. Zhong, Y. Huang, X. Wan, J. Peng, and J. Weng, "Nonlinear optical absorption of few-layer molybdenum diselenide (MoSe2) for passively mode-locked soliton fiber laser," Photonics Research **3**(2015).
29. Z. Luo, Y. Huang, M. Zhong, Y. Li, J. Wu, B. Xu, H. Xu, Z. Cai, J. Peng, and J. Weng, "1-, 1.5-, and 2-μm Fiber Lasers Q-Switched by a Broadband Few-Layer MoS2 Saturable Absorber," Journal of Lightwave Technology **32**, 4679-4686 (2014).
30. J. Sun, H. Shi, T. Siegrist, and D. J. Singh, "Electronic, transport, and optical properties of bulk and monolayer PdSe2," Applied Physics Letters **107**, 153902 (2015).
31. J. Ribeiro Soares, C. Janisch, Z. Liu, A. Elías, M. Dresselhaus, M. Terrones, L. Cançado, and A. Jorio, "Second Harmonic Generation in WSe 2," 2D Materials **2**, 045015 (2015).
32. C. Janisch, D. Ma, N. Mehta, A. Laura-Elias, N. Perea-Lopez, M. Terrones, and Z. Liu, "Harmonic generation in 2D layered materials," Proceedings of SPIE - The International Society

for Optical Engineering **9198**(2014).

33. X. Wen, Z. Gong, and D. Li, "Nonlinear optics of two-dimensional transition metal dichalcogenides," InfoMat **1**, 317-337 (2019).
34. M. Reichert, B. Turnbull, D. Fishman, H. Pattanaik, S. Webster, D. Hagan, and E. Van Stryland, *Extremely Non-Degenerate Two-Photon Emission in Direct-Gap Semiconductors* (2012), p. LTh2I.6.
35. E. Van Stryland, M. Woodall, H. Vanherzeele, and M. Soileau, "Energy bandgap dependence of two-photon absorption," Optics letters **10**, 490-492 (1985).
36. X. Yafeng, Z. Saifeng, L. Yuanxin, D. Ningning, Z. Xiaoyan, W. Lei, L. Weimin, M. K. Ivan, N. Jean-Michel, Q. Hongji, Z. Long, and W. Jun, "Layer-modulated two-photon absorption in MoS2: probing the shift of the excitonic dark state and band-edge," Photon. Res. **7**, 762-770 (2019).
37. K. Wang, J. Wang, J. Fan, M. Lotya, A. Gallagher, D. Fox, Y. Feng, X. Zhang, B. Jiang, Q. Zhao, H. Zhang, J. Coleman, L. Zhang, and W. Blau, "Ultrafast Saturable Absorption of Two-Dimensional MoS2 Nanosheets," ACS Nano **7**(2013).
38. C. Wei, H. Luo, H. Zhang, C. Li, J. Xie, J. Li, and Y. Liu, "Passively Q-switched mid-infrared fluoride fiber laser around 3 μm using a tungsten disulfide (WS2) saturable absorber," Laser Physics Letters **13**(2016).
39. S. Bikorimana, P. Lama, A. Walser, R. Dorsinville, S. Anghel, A. Mitioglu, A. Micu, and L. Kulyuk, "Nonlinear optical responses in two-dimensional transition metal dichalcogenide multilayer: WS2, WSe2, MoS2 and Mo0.5W0.5S2," Opt. Express **24**, 26998-26998 (2016).
40. B. Chen, X. Zhang, K. Wu, H. Wang, J. Wang, and J. Chen, "Q-switched fiber laser based on transition metal dichalcogenides MoS2, MoSe2, WS2, and WSe2," Opt. Express **23**, 26723-26737 (2015).
41. C. Ren, X. Deng, W. Hu, J. Li, X. Miao, S. Xiao, H. Liu, Q. Fan, K. Wang, and T. He, "A near-infrared I emissive dye: toward the application of saturable absorber and multiphoton fluorescence microscopy in the deep-tissue imaging window," Chemical Communications **55**, 5111-5114 (2019).

Figure caption

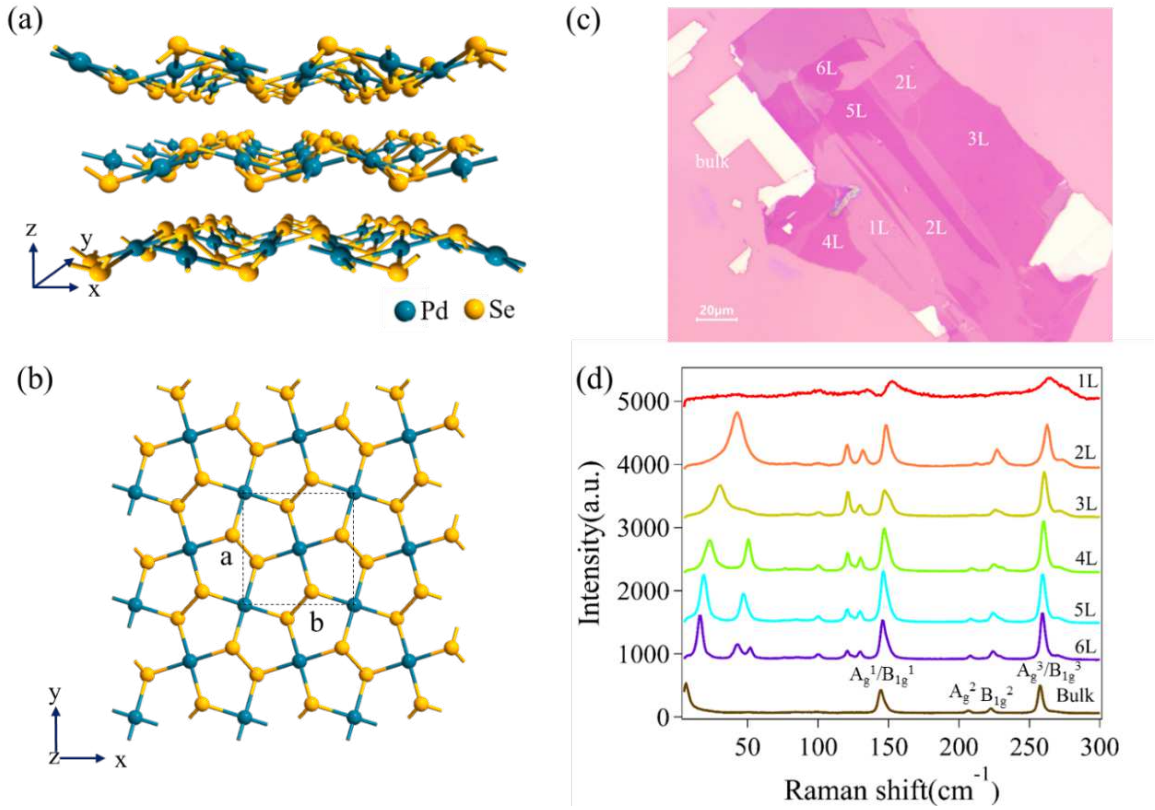

Figure 1. Crystallographic structure and optical characteristics of a few-layer $PdSe_2$. (a) The lattice structure of $PdSe_2$ flakes with puckered pentagonal. The unit cell vectors are denoted by the x, y, and z. Blue and yellow globes denote the Pd and Se atoms, respectively. (b) Top view of the atomic crystal structure of monolayer $PdSe_2$. The black dotted frame represents a unit cell of $PdSe_2$. The a and b denote the lattice constants in the x and y directions (the x and y directions are indicated in the left corner), respectively. (c) Optical microscope image of a few-layer $PdSe_2$ on the silicon substrate with a 285 nm SiO_2 layer. The number of sample layers containing 1-6 L was marked with white letters, and the scale bar is 20 μm. (d) Raman spectra of the 1-6 L and bulk $PdSe_2$ flakes with the same intensity axis. The low-frequency Raman peaks (0-100 cm^{-1}) are robust and even exceed that of the high-frequency modes. The Raman vibration modes of bulk $PdSe_2$ were marked, and they are the Ag^1, Ag^2, Ag^3, $B1g^1$, $B1g^2$, and $B1g^3$ mode, respectively.

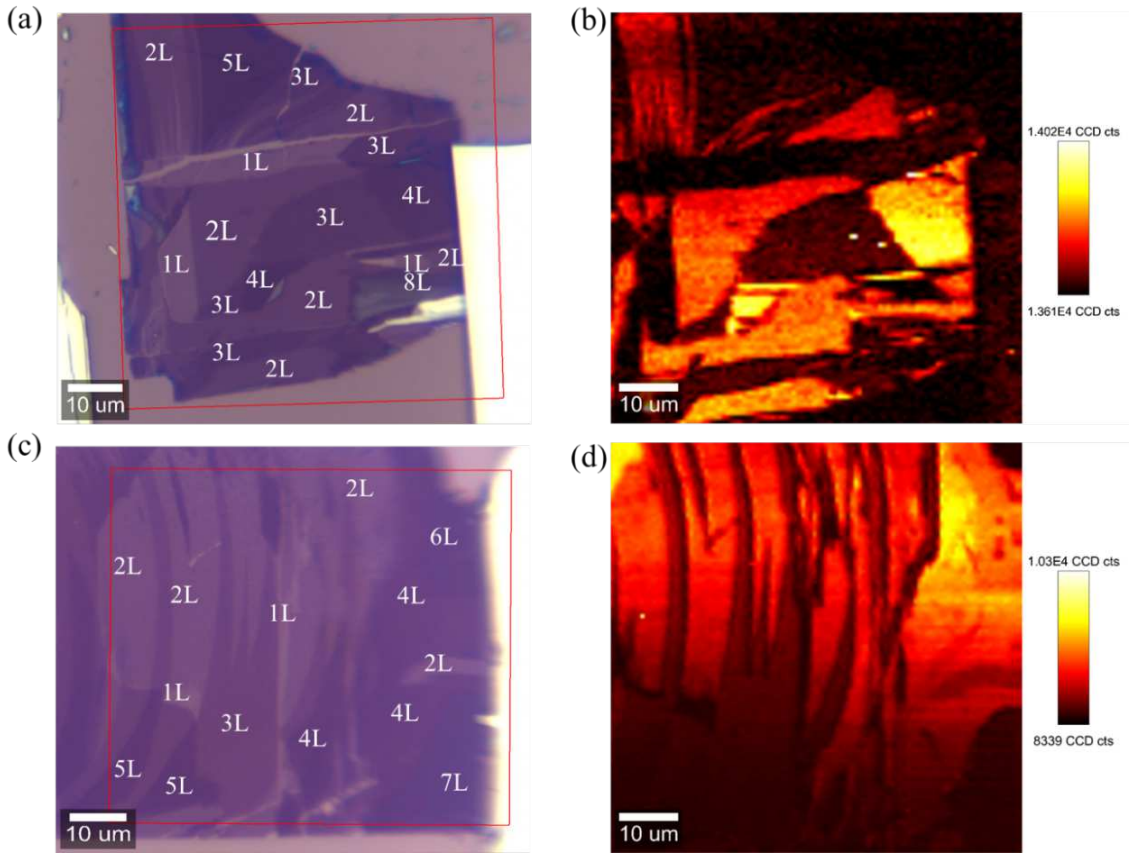

Figure 2. SHG spatial mapping of few-layer $PdSe_2$. (a, c) The optical image of the $PdSe_2$ flakes ready for the SHG characterization. The red boxes indicate the selected area for the SHG measurements. The layer number of the $PdSe_2$ sample is labeled by white letters. The 1-5 L and 8 L samples are contained in (a), and the 1-6 L samples are involved in (c), ensuring sufficient sampling. The $PdSe_2$ samples were excited under 800 nm wavelength under 50× objective with NA of 0.55. (b, d) The spatial mapping of the integrated SHG signal in the corresponding region in (a) and (c), respectively. The intensity of the SHG signal is different for different layers. The SHG signal is almost absent in the odd-layer samples, while it is strong in the even-layer samples. The color bars are shown on the right of the image, and the scale bars in the above graphs are all 10 μm.

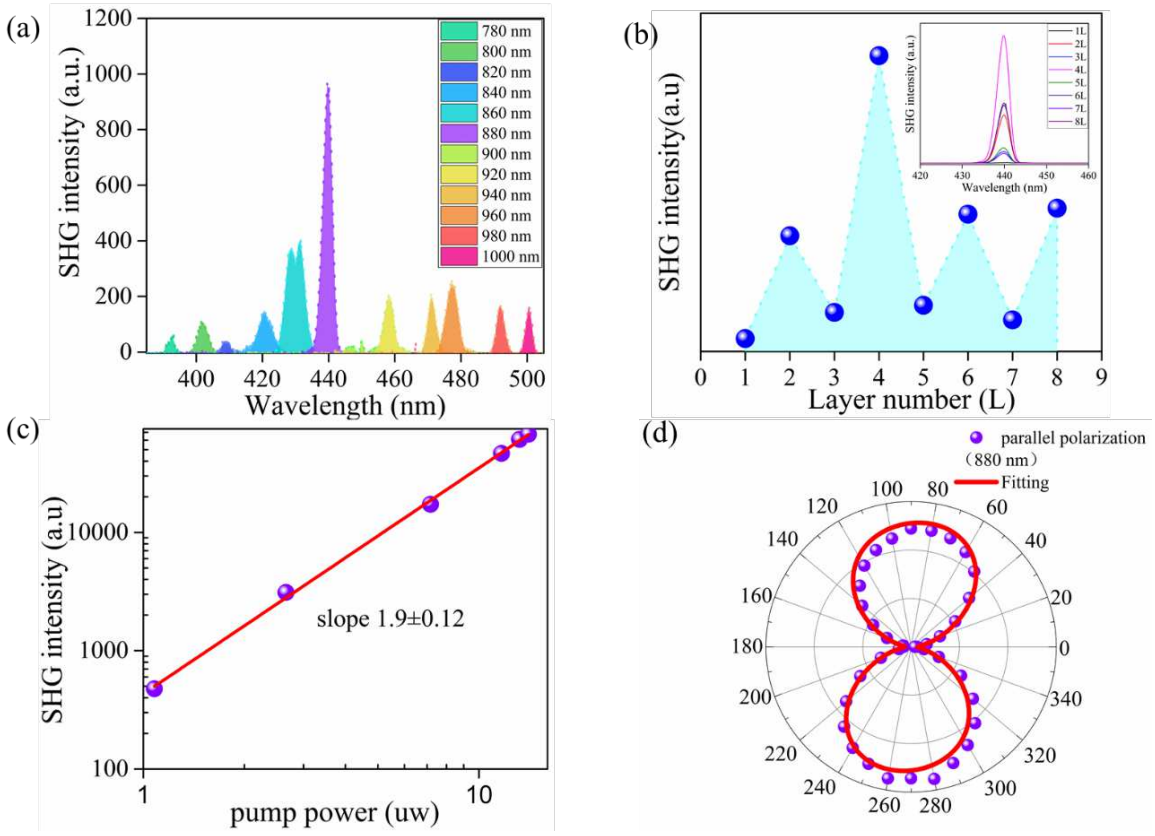

Figure 3. SHG characterizations of $PdSe_2$ flakes. (a) The SHG intensities excited at various wavelengths from 780~1000 nm, presented by the diverse colors. The highest intensity appears to be at the wavelength of 440 nm, manifesting the strongest SHG signal of excitation at 880 nm. (b) The SHG signal excited at the fixed wavelength of 880 nm in 1-8 L $PdSe_2$. The integrated intensity of SHG varies with different layers, represented by the blue dots. The SHG signal is the strongest in the 4 L sample. The inset represents the SHG intensities versus the layer number of $PdSe_2$. (c) The excitation power dependence of SHG intensities in 4 L $PdSe_2$. Both axes are shown on the log scale. The correlation of the pump power and SHG intensities exhibits to be linear, and the slope is 1.9±0.12. (d) Purple dots indicate the polar plot of integrated SHG intensities excited by the 880 nm laser in 4 L $PdSe_2$. The corresponding fitting result is denoted by the solid red curve.

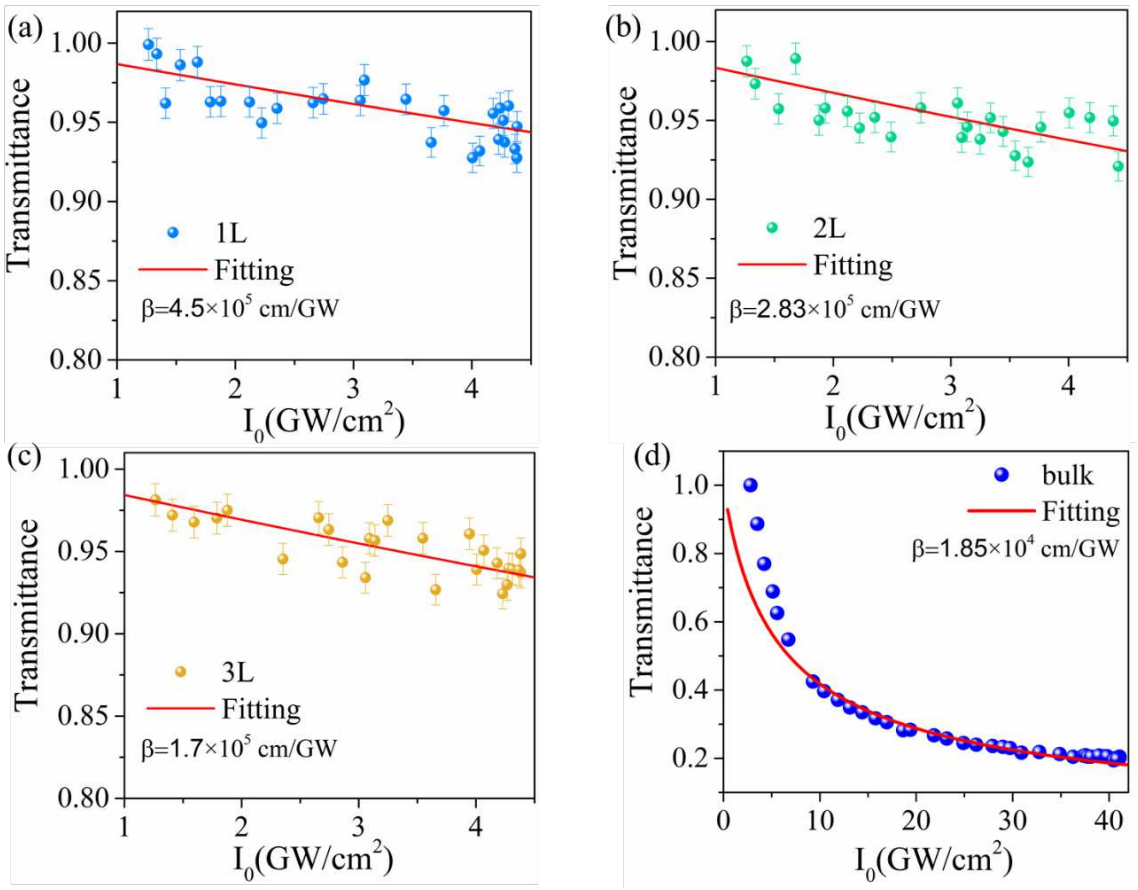

Figure 4. TPA properties of 1-3 L and bulk $PdSe_2$ flakes. (a-c) Nonlinear transmittance of 1-3 L $PdSe_2$. The blue, green, and yellow dots represent the experimental data, while the solid red lines indicate the fitted results using the TPA model. The TPA coefficients (β) of 1, 2, and 3 L $PdSe_2$ are 4.5×10^5, 2.83×10^5, and 1.7×10^5 cm/GW, respectively. (d) Nonlinear transmittance of bulk $PdSe_2$. The blue dots represent the experimental results, while the solid red lines indicate the fitted results using the TPA model. The nonlinear absorption coefficient (β) of bulk $PdSe_2$ is 1.85×10^4 cm/GW. The fitted results exhibit the reverse saturation absorption features. All the above measurements are performed under 800 nm excitation.

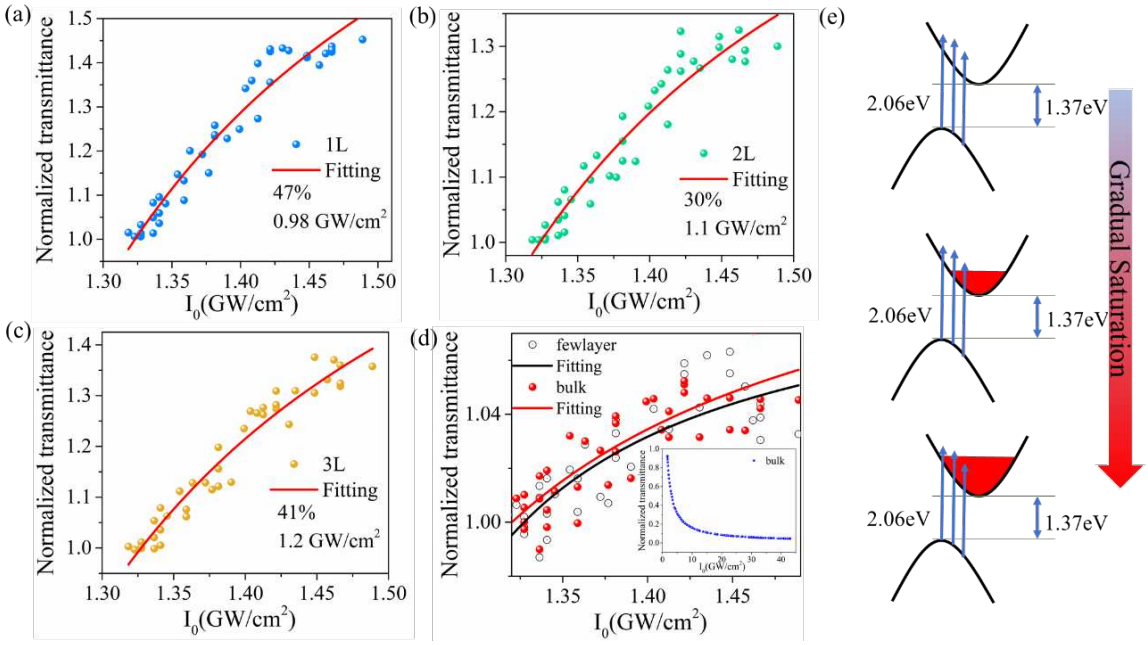

Figure 5. SA properties of 1-3 L and bulk $PdSe_2$ flakes. (a-c) Nonlinear transmittance of 1-3 L $PdSe_2$. The blue, green, and yellow dots represent the experimental data, while the solid red lines indicate the fitted results using the SA model. The SA intensities of 1, 2, and 3 L $PdSe_2$ are 0.98, 1.1, and 1.2 GW/cm^2, respectively. The modulation depth of 1, 2, and 3 L $PdSe_2$ are 47%, 30%, and 41%, respectively. (d) Nonlinear transmittance of bulk $PdSe_2$. The white and red dots represent the experimental data, while the black and red solid lines indicate the fitting curves of few-layer and bulk $PdSe_2$ using the SA model. The inset shows a reverse SA trend of the thick bulk $PdSe_2$ with increased laser power. (e) The electronic transition process of SA. All the above measurements are performed under 600 nm excitation.

Figures

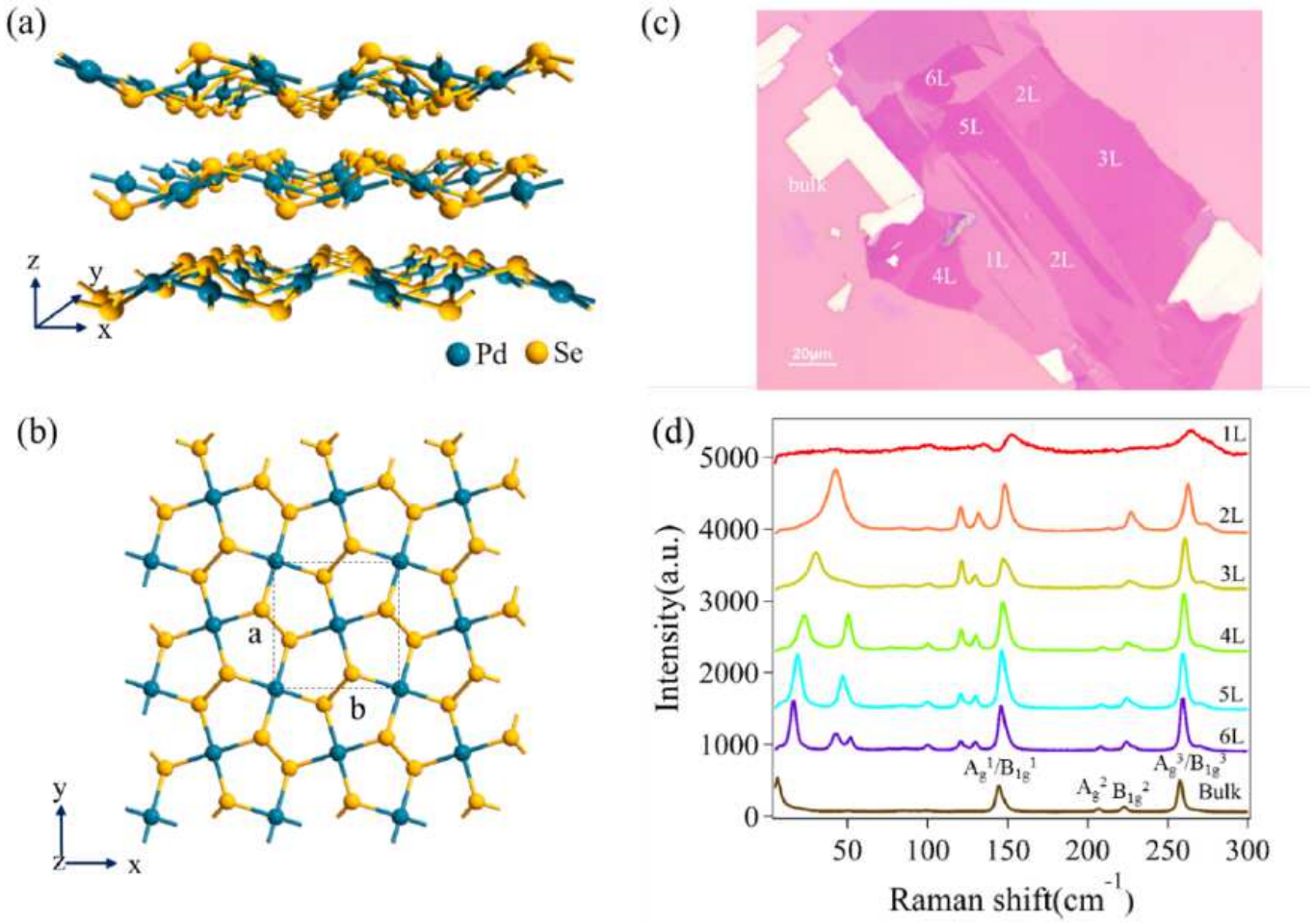

Figure 1

Crystallographic structure and optical characteristics of a few-layer PdSe2. (a) The lattice structure of PdSe2 flakes with puckered pentagonal. The unit cell vectors are denoted by the x, y, and z. Blue and yellow globes denote the Pd and Se atoms, respectively. (b) Top view of the atomic crystal structure of monolayer PdSe2. The black dotted frame represents a unit cell of PdSe2. The a and b denote the lattice constants in the x and y directions (the x and y directions are indicated in the left corner), respectively. (c) Optical microscope image of a few-layer PdSe2 on the silicon substrate with a 285 nm SiO2 layer. The number of sample layers containing 1-6 L was marked with white letters, and the scale bar is 20 μm. (d) Raman spectra of the 1-6 L and bulk PdSe2 flakes with the same intensity axis. The low-frequency Raman peaks (0-100 cm- 1) are robust and even exceed that of the high-frequency modes. The Raman vibration modes of bulk PdSe2 were marked, and they are the Ag1, Ag2, Ag3, B1g1, B1g2, and B1g3 mode, respectively.

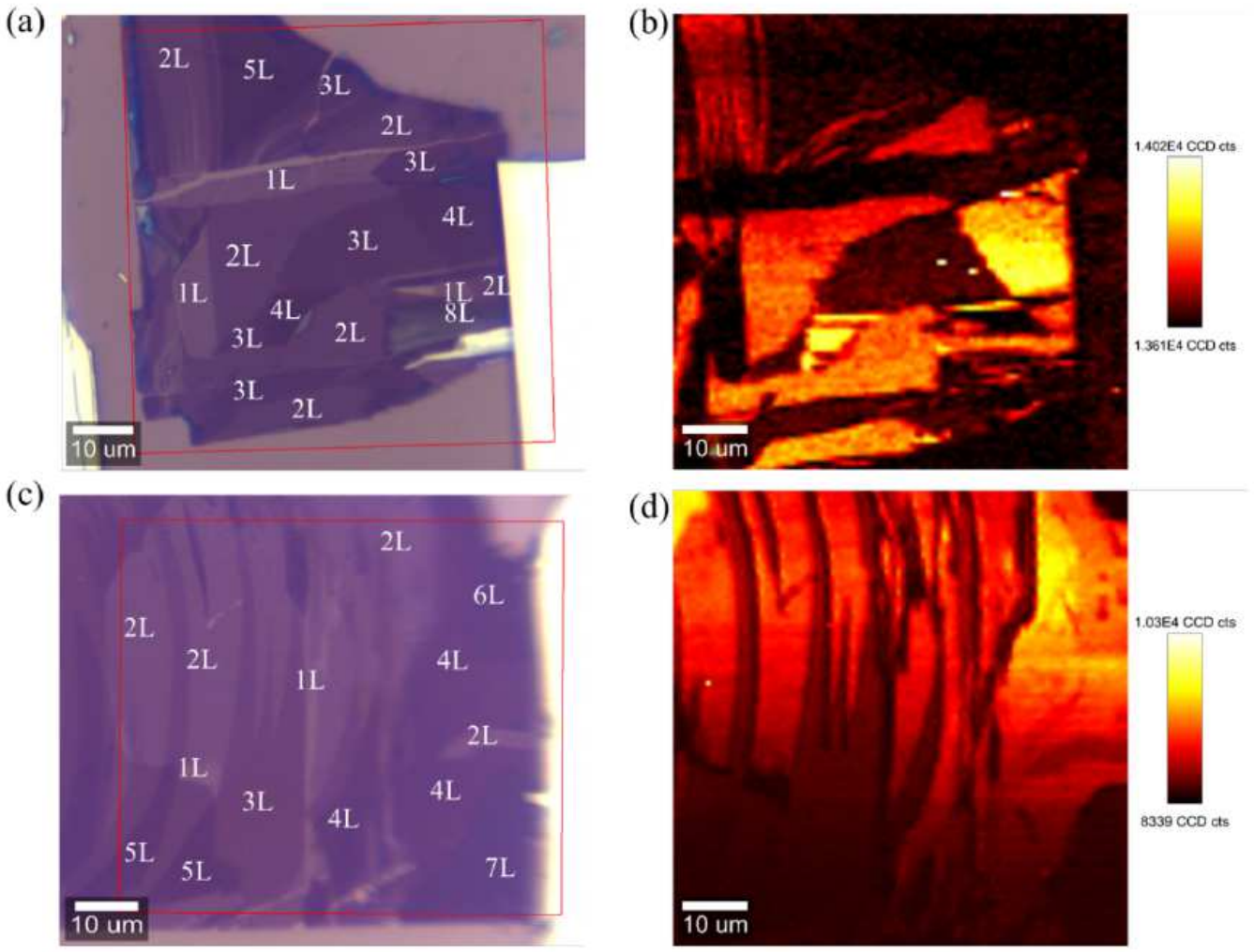

Figure 2

SHG spatial mapping of few-layer PdSe2. (a, c) The optical image of the PdSe2 flakes ready for the SHG characterization. The red boxes indicate the selected area for the SHG measurements. The layer number of the PdSe2 sample is labeled by white letters. The 1-5 L and 8 L samples are contained in (a), and the 1-6 L samples are involved in (c), ensuring sufficient sampling. The PdSe2 samples were excited under 800 nm wavelength under 50× objective with NA of 0.55. (b, d) The spatial mapping of the integrated SHG signal in the corresponding region in (a) and (c), respectively. The intensity of the SHG signal is different for different layers. The SHG signal is almost absent in the odd-layer samples, while it is strong in the even-layer samples. The color bars are shown on the right of the image, and the scale bars in the above graphs are all 10 μm.

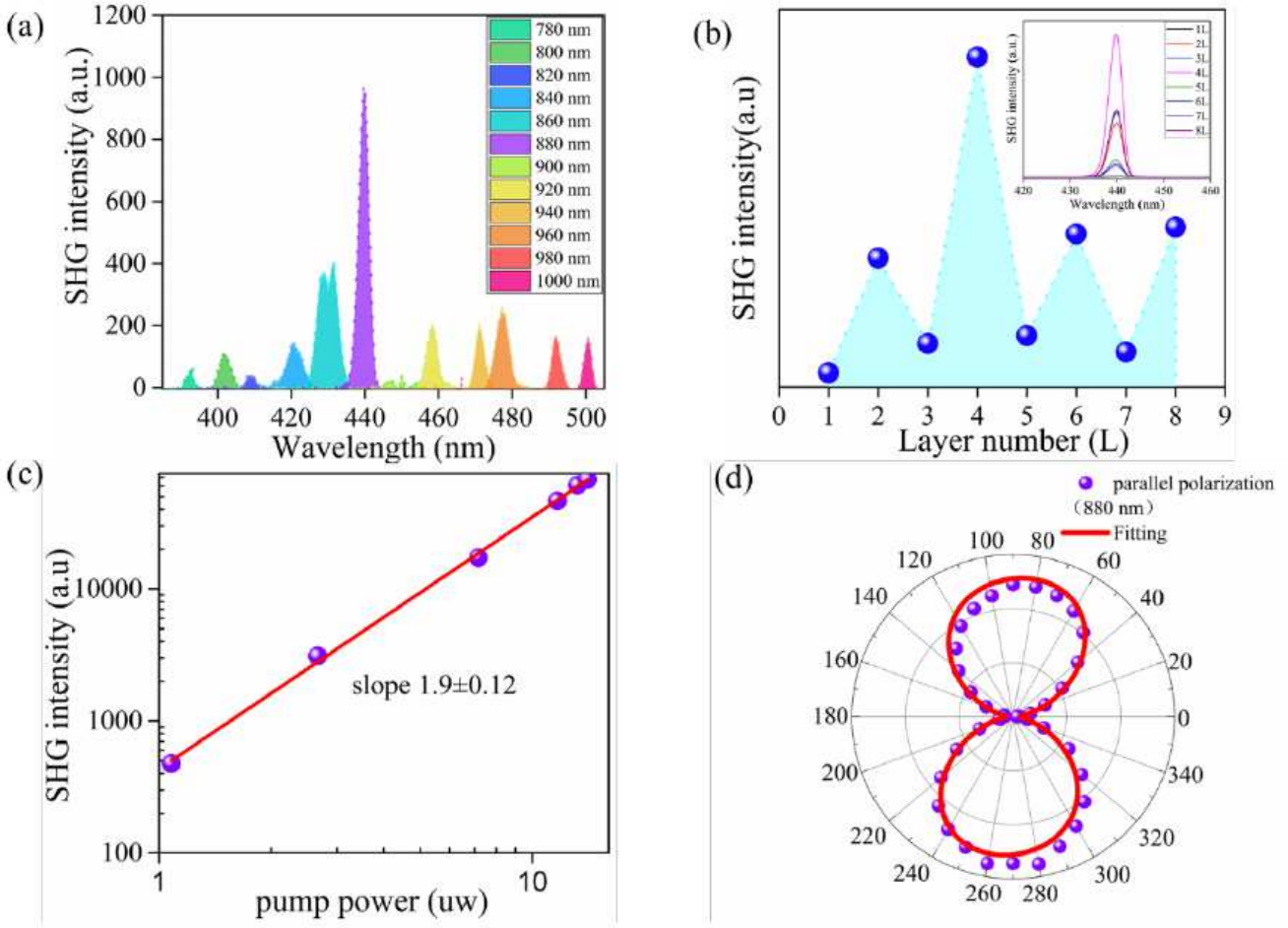

Figure 3

SHG characterizations of PdSe2 flakes. (a) The SHG intensities excited at various wavelengths from 780~1000 nm, presented by the diverse colors. The highest intensity appears to be at the wavelength of 440 nm, manifesting the strongest SHG signal of excitation at 880 nm. (b) The SHG signal excited at the fixed wavelength of 880 nm in 1-8 L PdSe2. The integrated intensity of SHG varies with different layers, represented by the blue dots. The SHG signal is the strongest in the 4 L sample. The inset represents the SHG intensities versus the layer number of PdSe2. (c) The excitation power dependence of SHG intensities in 4 L PdSe2. Both axes are shown on the log scale. The correlation of the pump power and SHG intensities exhibits to be linear, and the slope is 1.9±0.12. (d) Purple dots indicate the polar plot of integrated SHG intensities excited by the 880 nm laser in 4 L PdSe2. The corresponding fitting result is denoted by the solid red curve.

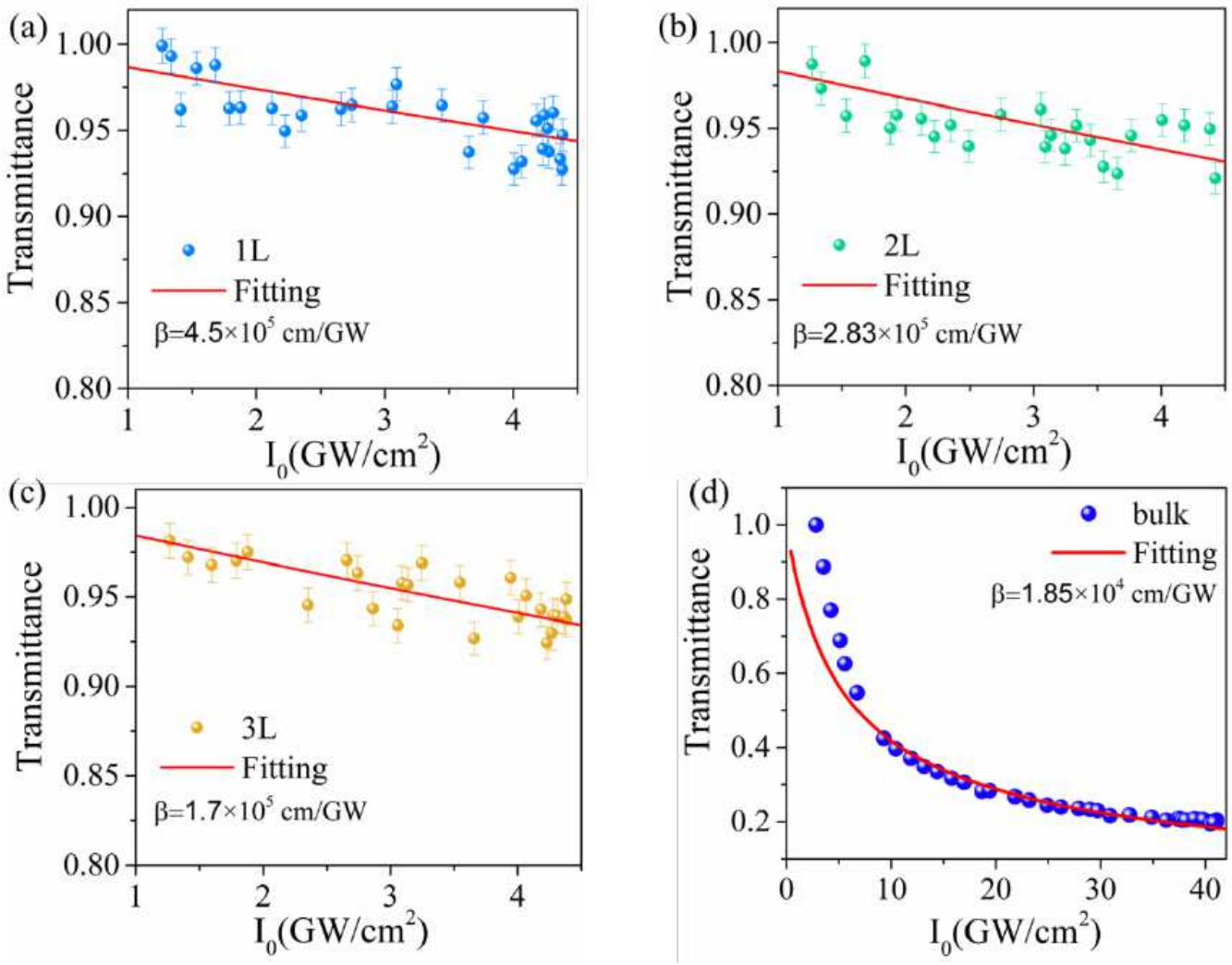

Figure 4

TPA properties of 1-3 L and bulk PdSe2 flakes. (a-c) Nonlinear transmittance of 1-3 L PdSe2. The blue, green, and yellow dots represent the experimental data, while the solid red lines indicate the fitted results using the TPA model. The TPA coefficients (β) of 1, 2, and 3 L PdSe2 are 4.5×105, 2.83×105, and 1.7 ×105 cm/GW, respectively. (d) Nonlinear transmittance of bulk PdSe2. The blue dots represent the experimental results, while the solid red lines indicate the fitted results using the TPA model. The nonlinear absorption coefficient (β) of bulk PdSe2 is 1.85× 104 cm/GW. The fitted results exhibit the reverse saturation absorption features. All the above measurements are performed under 800 nm excitation.

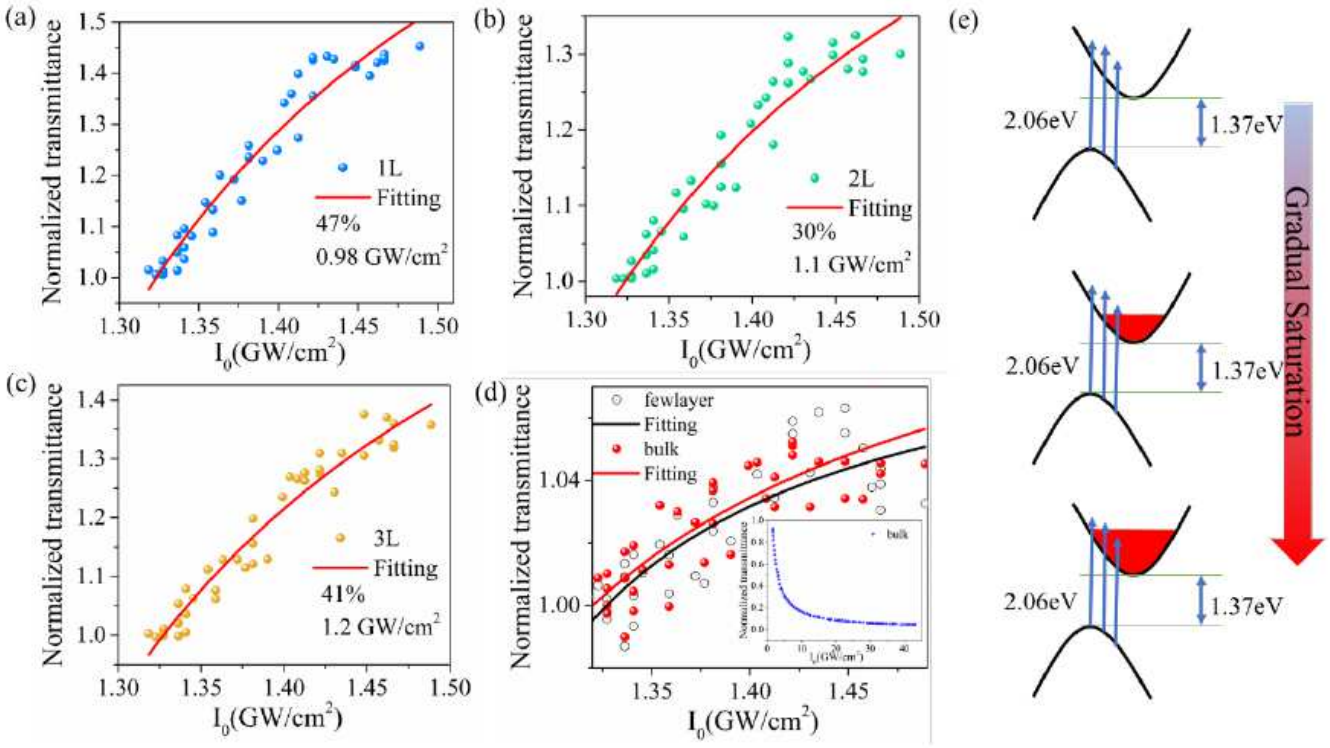

Figure 5

SA properties of 1-3 L and bulk PdSe2 flakes. (a-c) Nonlinear transmittance of 1-3 L PdSe2. The blue, green, and yellow dots represent the experimental data, while the solid red lines indicate the fitted results using the SA model. The SA intensities of 1, 2, and 3 L PdSe2 are 0.98, 1.1, and 1.2 GW/cm2, respectively. The modulation depth of 1, 2, and 3 L PdSe2 are 47%, 30%, and 41%, respectively. (d) Nonlinear transmittance of bulk PdSe2. The white and red dots represent the experimental data, while the black and red solid lines indicate the fitting curves of few-layer and bulk PdSe2 using the SA model. The inset shows a reverse SA trend of the thick bulk PdSe2 with increased laser power. (e) The electronic transition process of SA. All the above measurements are performed under 600 nm excitation.